HHS Public Access

Author manuscript

J Comp Neurol. Author manuscript; available in PMC 2019 July 01.

Published in final edited form as:

J Comp Neurol. 2018 July 01; 526(10): 1673–1689. doi:10.1002/cne.24437.

Morphological characterization of HVC projection neurons in the zebra finch (*Taeniopygia guttata*)

Sam E. Benezra[1,2,#], **Rajeevan T. Narayanan**[3,4,#], **Robert Egger**[1,2,4], **Marcel Oberlaender**[3,4], and **Michael A. Long**[1,2]

[1]NYU Neuroscience Institute and Department of Otolaryngology, New York University Langone Medical Center, New York, NY 10016 USA

[2]Center for Neural Science, New York University, New York, NY, 10003 USA

[3]Max Planck Group: In Silico Brain Sciences, Center of Advanced European Studies and Research, 53175 Bonn, Germany

[4]Computational Neuroanatomy Group, Max Planck Institute for Biological Cybernetics, 72076 Tübingen, Germany

Abstract

Singing behavior in the adult male zebra finch is dependent upon the activity of a cortical region known as HVC (proper name). The vast majority of HVC projection neurons send primary axons to either the downstream premotor nucleus RA (primary motor cortex) or Area X (basal ganglia), which play important roles in song production or song learning, respectively. In addition to these long-Crange outputs, HVC neurons also send local axon collaterals throughout that nucleus. Despite their implications for a range of circuit models, these local processes have never been completely reconstructed. Here we use *in vivo* single-Cneuron Neurobiotin fills to examine 40 projection neurons across 31 birds with somatic positions distributed across HVC. We show that $HVC_{(RA)}$ and $HVC_{(X)}$ neurons have categorically distinct dendritic fields. Additionally, these cell classes send axon collaterals that are either restricted to a small portion of HVC ("local neurons") or broadly distributed throughout the entire nucleus ("broadcast neurons"). Overall, these processes within HVC offer a structural basis for significant local processing underlying behaviorally-Crelevant population activity.

Graphical abstract

*To whom correspondence should be addressed: Michael A. Long (mlong@med.nyu.edu), 522 First Ave., SML 604, New York, NY 10016, P: (212) 263-9145; F: (212) 263-9120.

#these authors contributed equally

Benezra et al. used *in vivo* 2-photon targeted labeling to completely reconstruct 1 the local axonal 2 collaterals of the two major projection cell types in the vocal control nucleus HVC of male zebra 3 finches, helping to reveal the impact of single neurons on the generation of song-related neural 4 sequences.

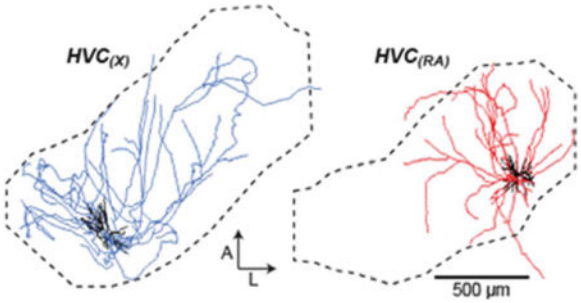

Keywords

songbird; vocal production; sequence generation; premotor; axon collaterals; RRID:SCR_014305 (Amira 3D analysis)

INTRODUCTION

The HVC nucleus of the zebra finch telencephalon is a crucial link in the song production pathway, sending descending projections from the forebrain to the brainstem and ultimately driving muscles important for vocal production (Bottjer, Glaessner, & Arnold, 1985; Goller & Cooper, 2004; Nottebohm, Kelley, & Paton, 1982; Nottebohm, Stokes, & Leonard, 1976; Wild, 1993). Within that region, the premotor cell population that projects to the downstream motor cortical region RA (robust nucleus of the arcopallium) are referred to as $HVC_{(RA)}$ neurons. Additionally, another group of cells ($HVC_{(X)}$ neurons) project to the avian basal ganglia (Dutar, Vu, & Perkel, 1998; Kubota & Taniguchi, 1998; Mooney, 2000). $HVC_{(X)}$ neurons are thought to be critical for song acquisition during development (Scharff, Kirn, Grossman, Macklis, & Nottebohm, 2000; Scharff & Nottebohm, 1991; Sohrabji, Nordeen, & Nordeen, 1990), but the role of these neurons in the production and maintenance of adult song is less well understood (Scharff et al., 2000). During singing, both HVC projection neuron types exhibit sparse bursts that form sequences of activity at the network level, with different neurons precisely active at different moments throughout the song (Hahnloser, Kozhevnikov, & Fee, 2002; Hamaguchi, Tschida, Yoon, Donald, & Mooney, 2014; Kozhevnikov & Fee, 2007; Long, Jin, & Fee, 2010; Lynch, Okubo, Hanuschkin, Hahnloser, & Fee, 2016; Picardo et al., 2016; Vallentin & Long, 2015). The importance of local processing within HVC for the generation of these neural sequences remains controversial, in part because the structure of circuits within HVC are only partially understood (Kornfeld et al., 2017; Kosche, Vallentin, & Long, 2015; Mooney & Prather, 2005; Stauffer et al., 2012).

A major gap in our knowledge of HVC function stems from an incomplete picture of the local wiring within that nucleus, especially with respect to the axon collaterals of excitatory projection neurons. These local processes have been shown to form interconnections within HVC (Kornfeld et al., 2017; Kosche et al., 2015; Mooney & Prather, 2005) and have been strongly implicated in the generation of sequences of neural activity (Galvis, Wu, Hyson, Johnson, & Bertram, 2017; Gibb, Gentner, & Abarbanel, 2009; Hanuschkin, Diesmann, & Morrison, 2011; Jin, 2009; Long et al., 2010). Although the basic morphological

characteristics of HVC neurons have been investigated through bulk labeling (Benton, Cardin, & DeVoogd, 1998; Fortune & Margoliash, 1995; Nixdorf, Davis, & DeVoogd, 1989; Vates, Broome, Mello, & Nottebohm, 1996; Yip, Miller-Sims, & Bottjer, 2012) or partially reconstructed single-cell fills (Dutar et al., 1998; Katz & Gurney, 1981; Mooney, 2000), surprisingly little is known about their anatomy because these reconstructions were incomplete. To better understand the impact of single neurons within the circuit, we generated the first complete reconstructions of HVC projection neuron morphology through *in vivo* single-cell labeling and cell tracing within the entire volume of HVC. From these reconstructions, we characterize dendritic morphology of individual neurons as well as a wide range of projection patterns of axon collaterals that extend throughout the volume of that structure. Both $HVC_{(RA)}$ and $HVC_{(X)}$ neurons have significant local axonal projections, whose projection patterns form a basis for local processing within this sequence-generating cortical circuit.

MATERIALS AND METHODS

Animals

We used adult (>90 days post hatch) male zebra finches that were obtained from an outside breeder and maintained in a temperature- and humidity-controlled environment with a 12/12 hr light/dark schedule. All animal maintenance and experimental procedures were performed according to the guidelines established by the Institutional Animal Care and Use Committee at the New York University Langone Health.

Surgery

To conduct 2-photon guided cell labeling, we employed a previously described *in vivo* microscopy preparation (Kornfeld et al., 2017). Briefly, animals were anesthetized with 1-3% isoflurane in oxygen, and a retrograde dextran tracer conjugated to Tetramethylrhodamine (fluoro-Ruby, MW: 10,000; Invitrogen) was injected into either RA or Area X. To gain optical access to HVC, a craniotomy (1mm × 1mm) was prepared using stereotaxic coordinates, the dura was removed, and a cover glass (#0 thickness, Warner Instruments, Hamden, CT) was implanted over the exposed brain with dental acrylic (Cooralite Dental MFG, Diamond Springs, CA). A small metal head plate with two tapped holes was implanted at the anterior part of the skull using dental acrylic to enable head fixation during 2-photon imaging.

2-Photon guided cell labeling

All cell fills were conducted while the animal was anesthetized (1.5% isoflurane in oxygen). On the day of the experiment, a region of dense retrograde labeling in HVC was defined using 2-photon microscopy (MOM, Sutter Instrument Company), and a small pipette access hole was drilled in the cover glass adjacent to this region. In each animal, 1-2 cells were targeted under 2-photon guidance and loaded with 3% Neurobiotin (Vector Labs, Burlingame, CA) in 150 mM K-Gluconate using a glass electrode (4–6 MΩ) in a juxtacellular configuration by applying 250 ms current pulses (2-15 nA; 2 Hz) for ~10 minutes (Kornfeld et al., 2017; Narayanan et al., 2014; Pinault, 1996). Pipettes were visualized by adding 40 μM of Alexa 488 (Invitrogen) to the internal solution. The activity

of $HVC_{(RA)}$ and $HVC_{(X)}$ neurons was monitored during the fill process using a Multiclamp 700B amplifier (Molecular Devices). Successful Neurobiotin loading was often accompanied by transfer of the Alexa fluorophore into the cell body, providing visual confirmation. Following single-cell dye injection, the pipette was slowly withdrawn from the cell and removed from the brain. Kwik-Cast (World Precision Instruments) was then applied over the exposed tissue and the animal was removed from anesthesia.

Histological procedures

After 1–3 hours following the completion of juxtacellular filling, birds were anesthetized with pentobarbital sodium and perfused transcardially with 4% w/v paraformaldehyde (EMS). Brains were removed from the skull using a surgical scoop, immersed in 4% paraformaldehyde for 3-5 days to achieve thorough fixation, and incubated in phosphate buffer for an additional 1–3 days to decrease endogenous peroxidase activity. To prepare sections, the brain was cut along the midline, mounted on the sagittal surface with cyanoacrylate, and stabilized with 3% agarose. Parasagittal sections (100 μm thickness) of HVC were cut using a vibratome (Leica VT1000S). Slices were washed five times with phosphate buffer and treated with 3% H_2O_2 to further reduce endogenous peroxidase activity. Slices were then immersed overnight at 4°C in a solution containing avidin/biotin complexes and 0.5% Triton X-100 in phosphate buffer (Vector Labs and Sigma-Aldrich, respectively) to tag the Neurobiotin with peroxidase complex. On the following day, slices were washed five times with phosphate buffer and then immersed in a solution containing 2.3 mM diaminobenzidine (DAB, Sigma-Aldrich) and 0.01% H_2O_2 in phosphate buffer to label processes containing Neurobiotin. Slices were then washed and mounted on slides with Vectashield (Vector Labs) or Mowiol (Sigma-Aldrich) mounting medium.

Post-histological imaging and reconstruction

A full description of our imaging and reconstruction procedures was published previously (Kornfeld et al., 2017). Only well-filled $HVC_{(RA)}$ neurons were selected for reconstruction, specifically those in which the soma, dendrite, and axon were all labeled without interruptions and with clearly labeled dendritic spines and presynaptic boutons. The cells that passed these criteria were imaged using light microscopy with a custom-designed high-resolution mosaic/optical-sectioning brightfield microscope system (Oberlaender, Bruno, Sakmann, & Broser, 2007; Oberlaender et al., 2009). Neuronal branches in each histological section were reconstructed in 3D using NeuroMorph (Oberlaender et al., 2007). Reconstructions were performed without prior knowledge about the projection target (apart from the descending axon), and branches were designated as belonging to axons or dendrites based on the presence of boutons or spines, respectively. Automated tracing results from each histological section were manually proof-edited using FilamentEditor (Dercksen, Hege, & Oberlaender, 2014), a custom-designed program based on Amira visualization software (FEI-Visualization Sciences Group). The NeuroMorph and FilamentEditor tools enable tracings that are independent of the experience of the human operator, with an inter-observer variability of approximately 20 μm per 1 mm axonal length (Dercksen et al., 2014).

Visualization and analysis of reconstructions

Light micrographs were captured using the microscope described in the previous section or a Zeiss AxioObserver Inverted SK-2. All visual renderings of reconstructed dendrites and axons were generated in Amira. Polar plots were generated by computing the total axonal length in 20-degree angular bins centered on the soma of each neuron reconstruction.

To generate an average HVC reference frame, we first manually traced HVC contours of all animals used in this study using microscope images (AX70, 10× objective UPlanFl) of the fluorescence of retrogradely labeled HVC projection neurons in all sagittal sections containing HVC. Contours were aligned across sections by spacing them 100 μm apart along the mediolateral axis, and aligning by translations and rotations in the sagittal plane using traced neuron morphology, blood vessels and the brain surface as references. The aligned HVC contours were then used to compute a closed surface by 3D Delaunay triangulation and defined as the HVC boundary surface. Next, we computed the center of mass and the three principal axes of the HVC boundary surface of each animal, and aligned the boundary surfaces of all animals using these coordinates and orientations. The extent of the HVC boundary surface along the three principal axes was defined as follows: For the first and second principal axes (i.e., the long axis, corresponding approximately to the mediolateral axis, and the medium axis, corresponding approximately to the anterior-posterior axis), the boundary surface was intersected with a plane centered on the center of mass and the plane normal defined by the direction of the third principal axis (i.e., the shortest axis, corresponding approximately to the dorsal-ventral axis). The maximum extent of the resulting intersection contour was then computed along the first and second principal axis, respectively. For the third principal axis, the boundary surface was intersected with a plane defined by the center of mass and the first principal axis. Finally, each neuron morphology was translated and rotated according to the center of mass and principal axes of the corresponding HVC boundary surface in the same animal, and variability in the extent of HVC along the three axes was minimized by scaling the neuron morphology linearly along each dimension according to the difference of the individual HVC boundary surface and the average extent along each axis. Finally, we transformed all aligned neuron morphologies to a coordinate system aligned with the anterior-posterior and mediolateral axes of the bird brain (Guest, Seetharama, Wendel, Strick, & Oberlaender, 2017). We measured the average angle between the first principal axis and the sagittal plane, as defined by the brain sections, and rotated all aligned neuron morphologies accordingly (i.e., by 28.5 degrees). For visualization purposes, we computed an average HVC boundary surface. We sampled all aligned HVC boundary surfaces every 50μm along the average extent of the first principal axis, and in 10 degree steps, computed the average location of these samples, and generated a closed boundary surface by 3D Delaunay triangulation.

Quantification of spatial parameters of dendrites and axons

For the following analyses, all axonal processes outside the boundaries of HVC were excluded. Total dendritic and axonal lengths were measured using the filament editor in Amira. “Primary branches” (Table 1) refers to the number of dendritic branches that emanate directly from the cell body. Branch nodes are bifurcation points along the dendrite or axon, and were quantified using the filament editor in Amira. One-dimensional spatial extent of

dendrites and axons were quantified in Amira, first by aligning the soma to the origin, then computing length in 10 or 50 μm voxels for dendrites and axons respectively, and plotting the distribution along the three principal axes. The radial dendritic extent was defined as the length of all dendrite segments in 1 μm thick concentric shells centered on the soma. HVC innervation proportion was computed for each cell by first replacing the line segments describing its axonal arbor by 100 μm radius tubes (i.e., reflecting the minimal average radius of potential postsynaptic projection neurons) (Table 1), yielding a closed surface (tube surface). The volume of the tube surface within the boundaries of HVC was measured, and was divided by the total volume of HVC in that animal. This yielded a number between 0 and 1 (HVC innervation proportion), which roughly reflects the fraction of HVC projection neurons whose dendritic fields are intersected by the axon. Differences in morphological properties between $HVC_{(RA)}$ and $HVC_{(X)}$ neurons were assessed using the Wilcoxon rank sum test.

Clustering of neurons based on dendritic and axonal projection patterns

To determine whether HVC projection neurons form morphologically defined clusters, we extracted parameters describing the 3D projection patterns of their dendrites and axons within HVC. For clustering of dendrites, we used four parameters: the 90% dendritic extent along the mediolateral and anterior-posterior axes within HVC, the 90% radial dendritic extent, and the total dendritic length. For clustering of axons, we used four parameters: the 90% axonal extent along the mediolateral and anterior-posterior axes within HVC, the HVC innervation proportion, and the total axonal length beyond 200 μm distance from the soma. Computing the 90% extent as opposed to the full extent made this analysis less sensitive to sparse outlier processes. Clustering of all neurons using dendrite and axon parameters occurred separately. We used the OPTICS algorithm (Ankerst, Breunig, Kriegel, & Sander, 1999; Oberlaender et al., 2012) to sort all neurons based on their mutual proximity in four-dimensional feature space. This allowed identifying groups of neurons forming regions of high density in feature space, which we identified as putative clusters. Neurons with low mutual proximity to neurons in these putative clusters were labeled as “ambiguous”. We decided to assign these “ambiguous” neurons to one of the two putative clusters based on their distance to the center of the two clusters, while accounting for potentially different variability within each cluster (Narayanan et al., 2015; Rojas-Piloni et al., 2017). Specifically, we defined the distance of neuron *i* to cluster *k* as:

$$d_{i,k} = \sqrt{(\vec{f}_i - \vec{\mu}_k)^T C_k^{-1} (\vec{f}_i - \vec{\mu}_k)}$$

Here, $\vec{f}_i$ is the four-dimensional feature vector of neuron *i*, $\vec{\mu}_k$ is the mean feature vector of cluster *k*, and C_k^{-1} is the inverse of the covariance matrix of cluster *k*. Hence, because we identified two putative clusters for each parameter set using the OPTICS algorithm, two distance values (i.e., one for each cluster) were computed for each “ambiguous” neuron. We then assigned each “ambiguous” neuron to the cluster with the smallest distance without requiring a predetermined cutoff distance.

RESULTS

To characterize the properties of local processes of HVC projection neurons, we conducted single-cell Neurobiotin fills (Narayanan et al., 2014; Pinault, 1996) *in vivo* under 2-photon guidance (Figure 1a–c; see Materials and Methods). In a total of 81 birds, we attempted to fill 59 $HVC_{(RA)}$ neurons and 34 $HVC_{(X)}$ neurons. Following histological processing and imaging (Figure 1d), we selected only the neurons whose dendrites and axons were completely and darkly labeled, a data set acquired from 31 birds and including 22 $HVC_{(RA)}$ neurons, 16 $HVC_{(X)}$ neurons, and 2 neurons projecting to both regions (Kittelberger, 2002). In this data set, we include 13 $HVC_{(RA)}$ neurons and 2 $HVC_{(RA/X)}$ neurons that were previously analyzed as part of a separate anatomical study (Kornfeld et al., 2017). As a population, the somata of the targeted cells spanned most of the mediolateral and rostrocaudal extent of HVC (Figure 1e). In contrast, their dorsal-ventral distribution was biased towards superficial neurons, due to limitations on imaging depth in our tissue (Figure 1f). For each neuron, we fully reconstructed all local processes including dendrites and axon collaterals (Figure 2). Long-range projections leading to RA and/or Area X were clearly visible in these neurons, enabling their identification. A single axon branch leading from HVC to RA often exited the posterior boundary of HVC (Figure 2a, e), while an axon branch from an $HVC_{(X)}$ neuron (Figure 2b, f) took a more variable path, exiting from the anterior, medial, or ventral boundary (Fortune & Margoliash, 1995). Additionally, three cells in our data set (one $HVC_{(RA)}$ and two $HVC_{(X)}$ neurons) sent two descending axon branches originating from the same hillock to the downstream nucleus.

$HVC_{(RA)}$ and $HVC_{(X)}$ neurons have distinct dendritic morphologies

Our approach enables us to visualize and reconstruct all neuronal processes of individual cells throughout the entire volume of HVC, thus avoiding any possible bias associated with analyzing partial reconstructions (Dutar et al., 1998; Fortune & Margoliash, 1995; Mooney, 2000). Our first step was to examine the dendrites of projection neurons in order to better understand the spatial extent of synaptic inputs that could arrive onto each cell type. Dendrites were similar in shape within a cell type, with dendritic arbors consistently more compact in $HVC_{(RA)}$ neurons than in $HVC_{(X)}$ neurons (Figure 3). We went on to quantify and compare the morphological properties of $HVC_{(RA)}$ and $HVC_{(X)}$ dendrites in several ways. First, to measure the span of dendrites we quantified and plotted the one-dimensional spatial extent of each arbor along the mediolateral, rostrocaudal, and dorsoventral axes (Table 1 and Figure 4a, b). We found that averaging across the population, $HVC_{(X)}$ dendrites have a 1.5-fold greater span than $HVC_{(RA)}$ dendrites in the mediolateral and dorsoventral axes, and a 2-fold greater span in the rostrocaudal axis. Across the population, $HVC_{(RA)}$ dendrites have a similar span in all three axes, lending to a spherical shape, while $HVC_{(X)}$ dendrites are slightly more elongated in the rostrocaudal axis (Table 1, Figure 4). We also measured total dendritic length of each cell, and found that $HVC_{(X)}$ dendrites on average have almost a 2-fold greater length than $HVC_{(RA)}$ dendrites (Table 1, Figure 4c). Averaging across the population, $HVC_{(X)}$ dendrites gave rise to an average of one more primary branches than $HVC_{(RA)}$ dendrites. The complexity of the dendritic arbor, as measured by the correlation between total path length and number of branch nodes, was similar across all neurons ($r = 0.78$, $p<10^{-6}$).

Our next step was to determine whether we could morphologically classify dendrites based on their spatial properties. We defined four parameters (total dendritic length, 90% extent along the mediolateral and anterior-posterior axis, and 90% radial extent, Figure 4a–c) and used a density-based cluster algorithm (Ankerst et al., 1999) to determine whether cells could be assigned to discrete groups (Oberlaender et al., 2012). Our analysis yielded two morphological categories, which appeared as distinct clusters in a principal component analysis (Figure 4d). One cluster consisted primarily of neurons with large dendritic fields, as measured by their radial extent, the extent across the three principal axes of HVC, and total path length (Table 1), and we hence referred to neurons in this cluster as “large”. The “large” cluster contained all $HVC_{(X)}$ neurons (see also Figure 3). $HVC_{(RA)}$ neurons – with one exception – were part of the remaining cluster, which we termed “small”, due to their compact dendritic span (Figure 3 and Table 1). In addition, one $HVC_{(RA/X)}$ neuron was assigned to each cluster.

Bouton morphology of local projections in HVC

After examining the dendritic structure of HVC projection neurons, we shifted our focus to potential presynaptic partners by examining local axonal boutons. Our first step was to assess the distribution of boutons along these wires, which correlate with the presence of presynaptic terminals (Kornfeld et al., 2017). Local collaterals of both $HVC_{(RA)}$ and $HVC_{(X)}$ neurons were lined with prominent swellings, which were readily visible along DAB-stained collaterals (Figure 5a). We manually counted boutons along collateral branches of 7 $HVC_{(RA)}$ and 9 $HVC_{(X)}$ neurons, and computed the bouton density of each branch (# of boutons/length of axon; Figure 5b). Across all branches, $HVC_{(RA)}$ and $HVC_{(X)}$ neurons had similar bouton densities ($HVC_{(RA)}$: 32 ± 2 Boutons/mm; $HVC_{(X)}$: 36 ± 2 Boutons/mm, mean ± SEM; Figure 5c), suggesting that they form connections with other neurons in HVC at similar frequencies. We previously reported that the density of boutons did not vary with soma distance in $HVC_{(RA)}$ neurons (Kornfeld et al., 2017), and found the same to be true for $HVC_{(X)}$ neurons (Pearson’s correlation $r = -0.20$; $p = 0.11$). However, boutons from both projection types appeared to sometimes be clustered (Figure 5a), which was further evident from nonuniform spatial distributions of boutons within an axon (Figure 5d).

Two categories of local axonal innervation

Once we confirmed that boutons are prevalent along collaterals, we moved on to examine and compare the structure of collaterals of $HVC_{(RA)}$ and $HVC_{(X)}$ neurons. In nearly all cells, collaterals were completely confined within the borders of HVC, even in cases where the soma was close to the edge of the nucleus (e.g., Figure 6, Cell 38). In two $HVC_{(X)}$ neurons, however, collateral branches extended outside of HVC and terminated approximately 500 μm rostral and caudal to the boundary of the nucleus, into HVC shelf (Kelley & Nottebohm, 1979). Cell 22 sent 7.2 mm of collaterals into rostral and caudal shelf, and Cell 103 sent 4.5 mm of collaterals into caudal shelf (Figures 7 and 9). A general feature of both projection types is that their local collaterals appeared to fill the dorsoventral extent of the nucleus. In the horizontal plane, however, an axon forming several collaterals emanated from the soma at distinctive orientations along the mediolateral and rostrocaudal axes (Figures 6–8). Across the population, we did not observe a clear bias toward a particular orientation relative to the soma. As with the dendrites, we observed almost a 2-fold greater total axon length of

$HVC_{(X)}$ neurons compared with $HVC_{(RA)}$ neurons, and the span of $HVC_{(X)}$ collaterals was larger along all measured dimensions (M-L, D-V, A-P) (Table 2).

Our next step was to determine if, like the dendrites, axon collaterals of HVC projection neurons could be organized into distinct morphological categories. We again focused specifically on parameters that describe the spatial properties of these projections and their innervation of HVC. For each cell, we quantified and plotted the one-dimensional spatial extent of the axon along the three principal axes (Table 2 and Figure 10a, b). We chose to exclude dorsoventral extent from our sorting analysis, as this parameter was relatively consistent from cell to cell (Table 2). We quantified distal axonal length (>200 μm Euclidean distance from soma), previously shown to preferentially target other projection neurons (Kornfeld et al., 2017) as a measure of broad axonal innervation, and used this as our third parameter (Figure 10c, left). Finally, for our fourth parameter, we computed an HVC innervation proportion for each cell (see Materials and Methods), which reflects the upper bound proportion of neurons in HVC whose dendritic fields overlap with the axonal field (Figure 10c, right). The cluster algorithm yielded two clusters distinguished by the span of their axonal fields, leading to morphological categories that we refer to as “local” and “broadcast” neurons (Figure 10d and Table 2). “Broadcast” neurons had a higher extent along all principal axes than “local” neurons (M-L: 1.6-fold higher; A-P: 1.5-fold higher; D-V: 1.3-fold higher; $p < 0.005$ in all cases), 1.9-fold more path length within HVC ($p = 1.0*10^{-4}$), and innervated a larger fraction of HVC (1.4-fold higher HVC innervation ratio, $p = 0.01$). In contrast to the dendrites, we found that “local” and “broadcast” neurons were not as strictly associated with projection type: The “local” group consisted of 21 $HVC_{(RA)}$, 6 $HVC_{(X)}$, and 1 HVC(RA/X), while the “broadcast” group consisted of 1 $HVC_{(RA)}$, 10 $HVC_{(X)}$ and 1 $HVC_{(RA/X)}$ (Figures 6–8). Therefore, 6 out of 16 $HVC_{(X)}$ neurons have similar axon morphologies to $HVC_{(RA)}$ neurons in terms of their spatial distribution within HVC, whereas 10 $HVC_{(X)}$ neurons exhibit distinctly broader projections that innervate a larger volume of HVC. To visualize and compare how “local” and “broadcast” neurons innervate HVC, we mapped the axons of three example neurons in each category onto an average geometrical reference frame (see Materials and Methods; Figure 11a, b). “Broadcast” axons occupy a relatively large volume and span most of the mediolateral and rostrocaudal extent of HVC, whereas the “local” axons are more spatially confined and occupy a smaller volume in the nucleus (Figure 11c, d, Table 2).

DISCUSSION

We used *in vivo* 2-photon guided single cell labeling to acquire a data set of 40 HVC projection neurons to examine the projection patterns of their dendrites and local axon collaterals in three dimensions. This data set contains the first complete reconstructions of local processes across the entire volume of HVC. By characterizing these morphological properties in detail, we have gained insight into the impact of individual neurons on the circuits involved in the acquisition and production of a well-characterized complex sensorimotor behavior.

2-photon targeted cell labeling

Our approach of using *in vivo* microscopy to assist cell targeting/filling enabled several experimental advantages. First, we were able to choose the cells we targeted based on their projection type by injecting a fluorescent retrograde tracer in either RA or Area X. Furthermore, by observing the field of retrogradely labeled neurons, we were able to target cells in specific regions of HVC, which made it easier to generate a data set that spanned the mediolateral and rostrocaudal extent of the nucleus. Second, the visualized approach helped to direct the tip of the electrode during the process of cell filling, which was especially useful when targeting $HVC_{(RA)}$ neurons, which have relatively small somata (7-10 μm diameter). Third, we were able to monitor the flow of internal solution from the pipette tip throughout the experiment, ensuring that it was not clogged before attempting to inject Neurobiotin. One limitation to this approach is that our fills are biased toward neurons in the dorsal half of HVC, as dextran-labeled neurons were only visible up to ~400 μm ventral from the surface, and the ventral-most boundary of HVC extends approximately ~550 μm ventral. It is possible that neurons closer to the ventral boundary send collaterals dorsally, mirroring what we observe from cells in our data set, however we cannot rule out the possibility that the collaterals of ventral neurons exhibit different projection patterns altogether.

$HVC_{(RA)}$ neurons: Functional implications for sequence generation

The primary function of $HVC_{(RA)}$ neurons is to provide premotor commands to the song production pathway (Nottebohm et al., 1976). During singing, the majority of $HVC_{(RA)}$ neurons are sparsely active at moments that are highly stereotyped across song renditions (Hahnloser et al., 2002). Different $HVC_{(RA)}$ neurons are often active at different time points, forming a sparse sequence that spans the entirety of the song (Hahnloser et al., 2002; Kozhevnikov & Fee, 2007; Lynch et al., 2016; Picardo et al., 2016). Several models have been proposed to explain how $HVC_{(RA)}$ premotor sequences are generated during singing. In one class of models, precisely timed bursts are the direct result of connectivity between $HVC_{(RA)}$ neurons, which have been proposed to form a feed-forward network (Long et al., 2010). An alternative model suggests that sequential activity may be generated by a distributed network involving structures outside HVC, where precisely timed bursts during song are driven by thalamic afferents onto $HVC_{(RA)}$ neurons rather than local connections within the nucleus (Hamaguchi, Tanaka, & Mooney, 2016).

Our current findings provide an anatomical basis for local excitatory connectivity that may play an important functional role within HVC. We show that nearly all 22 $HVC_{(RA)}$ cells have elaborate axon collaterals that exclusively innervate HVC and likely make many connections, as supported by the prevalence of putative presynaptic terminals. We were able to estimate the total boutons per $HVC_{(RA)}$ cell by multiplying the axonal length and bouton density. We find that, on average, an HVC(RA) neuron forms 401 ± 52 boutons. Given that there are approximately 40,000 $HVC_{(RA)}$ neurons (Walton, Pariser, & Nottebohm, 2012; Wang, Hurley, Pytte, & Kirn, 2002), we estimate that the entire population of $HVC_{(RA)}$ neurons forms approximately 16 million local boutons, suggesting a significant impact on network activity in HVC during song production.

To better understand the role of intrinsic HVC circuitry, we must first establish the postsynaptic partners of the $HVC_{(RA)}$ neurons, which cannot be determined through the light microscopic approach used in this study. Paired recordings *in vitro* have found sparse evidence for $HVC_{(RA)}$-$HVC_{(RA)}$ connections (Kosche et al., 2015; Mooney & Prather, 2005), motivating a number of alternative models in which disynaptic inhibition within HVC is sufficient to generate song related sequences (Armstrong & Abarbanel, 2016; Gibb et al., 2009). In a previous study, using an electron microscopic approach capable of revealing the identity of postsynaptic partners of $HVC_{(RA)}$ neurons, we found that 17% of synapses made by $HVC_{(RA)}$ axons form connections onto other $HVC_{(RA)}$ neurons (Kornfeld et al., 2017) and that the total density of these connections is approximately 75 synapses/mm (Kornfeld et al., 2017). With this data set, we update our previous estimate (Kornfeld et al., 2017) for the average axonal length of $HVC_{(RA)}$ collaterals (13.31 ± 1.44 mm mean ± SEM) by including data from an additional 9 neurons. We now estimate that each individual $HVC_{(RA)}$ neuron forms 170 ± 18 synapses onto other $HVC_{(RA)}$ neurons, which suggests that the synaptic connections exist to allow for the possibility that this feed-forward circuit architecture could enable the generation of song-related sequences within HVC. The total number of synaptic partners remains elusive, because little is known about the relative number of connections made between a given pair of $HVC_{(RA)}$ neurons (Kornfeld et al., 2017).

Additionally, in our previous study, we observed that $HVC_{(RA)}$-HVC(RA) connections often occurred in the portions of the axons that were distant from the soma. This regional specialization, coupled with the relatively compact nature of $HVC_{(RA)}$ axonal field, places specific spatial bounds on the location of $HVC_{(RA)}$ postsynaptic partners – proximal axons are not likely to form robust $HVC_{(RA)}$-HVC(RA) synapses and axons often do not reach across the entire span of the nucleus. Furthermore, we find that collaterals of both $HVC_{(RA)}$ and $HVC_{(X)}$ neurons are heterogeneously biased in orientation with respect to their soma, suggesting that excitatory signals during singing propagate without a bias toward a particular axis in HVC.

Our results are also relevant in light of previous data suggesting that HVC is composed of multiple processing centers with distinct behavioral roles. In these studies, microlesions to specific subregions of HVC led to selective deficits in song structure (Basista et al., 2014; Galvis et al., 2017). Despite these compelling findings, we were unable to see differences between the anatomical properties of individual premotor neurons across the extent of HVC. As a result, the differences observed following perturbation may result from other factors, such as the specific downstream targets of these neurons within RA, for instance. Additionally, functional observations (Stauffer et al., 2012) as well as perturbation studies (Poole, Markowitz, & Gardner, 2012; Stauffer et al., 2012) have suggested an anterior-posterior bias in the wiring of HVC. In our data set, axonal collaterals sometimes send significant projections in the mediolateral direction (e.g., Figure 6), indicating the existence of long-range connectivity across the long axis of HVC. Future studies using more precise methods to monitor and perturb these long-range axonal collaterals may hold the key to understanding their role.

$HVC_{(X)}$ neurons: Local processing of basal-ganglia projecting neurons within HVC

$HVC_{(X)}$ neurons project to the avian basal ganglia and are primarily involved in delivering an efference copy of motor activity to the anterior forebrain pathway. Although $HVC_{(X)}$ neurons are essential for song learning (Scharff & Nottebohm, 1991; Sohrabji et al., 1990), their role in adult song production is less clear (Scharff et al., 2000). Our study suggests four potentially new roles for the $HVC_{(X)}$ network. First, the possibility exists that $HVC_{(X)}$ neurons may have an impact on vocal production in adult zebra finches, given the fact that $HVC_{(X)}$ neurons have such an extensive network of axon collaterals in HVC. Considering the average total axon collateral length and bouton density of $HVC_{(X)}$ neurons, we estimate that on average, an $HVC_{(X)}$ neuron forms 755 ± 91 boutons. There are approximately 10,000 $HVC_{(X)}$ neurons in the nucleus (Walton et al., 2012), so the population of $HVC_{(X)}$ neurons may form approximately 7.5 million boutons in HVC. Given that $HVC_{(X)}$ neurons display activity patterns similar to $HVC_{(RA)}$ neurons during song production (Hahnloser et al., 2002; Long et al., 2010; Vallentin & Long, 2015) and may form many connections with $HVC_{(RA)}$ neurons, despite a paucity of such interconnections having been observed in earlier studies (Mooney & Prather, 2005). Future work is needed to determine whether $HVC_{(X)}$ neurons play a role in the premotor patterns leading to the generation of singing behavior. Second, we find that $HVC_{(X)}$ neurons can exist either as ‘local’ or ‘broadcast’ neurons. Future functional measurements of these neurons during singing combined with anatomical reconstructions could potentially shed light on the roles of different morphological classes in song production. Third, we found a subpopulation of $HVC_{(X)}$ neurons that innervate a region adjacent to HVC, known as HVC shelf (Kelley & Nottebohm, 1979). HVC shelf is an auditory region that receives input from field L (Fortune & Margoliash, 1995; C. V. Mello, Vates, Okuhata, & Nottebohm, 1998; Vates et al., 1996), which is the primary forebrain relay for pathways originating in the auditory thalamus (Bonke, Bonke, & Scheich, 1979; Fortune & Margoliash, 1992; Karten, 1968). Therefore, the $HVC_{(X)}$-to-shelf synapse could be transmitting motor-related signals to the auditory system, similar to a recently characterized population of HVC neurons projecting to Avalanche (Roberts et al., 2017). Fourth, two HVC neurons send long-range projections to both X and RA. Such dual projectors have been previously described in one existing data set (Kittelberger, 2002), but the unique function of such neurons – if any – remains elusive. In our study, we present two such neurons and further find that one neuron appears to have morphological similarities to $HVC_{(X)}$ neurons and the other appears more similar to an $HVC_{(RA)}$ neuron (Rojas-Piloni et al., 2017). Whether $HVC_{(RA/X)}$ neurons are an example of errant wiring or a distinct neuron cell type with a specified functional role within the network remains unknown.

In conclusion, we show that there is significant innervation within HVC from both major projection cell types, providing the substrate for local processing that could potentially play a crucial role in vocal learning and production. Furthermore, these connections can help to inform our understanding of the neural mechanisms of sequence generation more broadly (Harvey, Coen, & Tank, 2012; G. B. Mello, Soares, & Paton, 2015; Pastalkova, Itskov, Amarasingham, & Buzsaki, 2008; Schmidt et al., 2017; Schmitt et al., 2017).

Acknowledgments

This research was supported by the NIH (R01NS075044) (M.L.), the New York Stem Cell Foundation (M.L.), the Rita Allen Foundation (M.L.), Simons Foundation (Global Brain Initiative) (M.L.), the German Research Foundation (DFG) EG 401/1C1 (R.E), EMBO ALTF 348C2017 (R.E.), the Center of Advanced European Studies and Research (caesar, M.O.), the Max Planck Institute for Biological Cybernetics (M.O.), the Bernstein Center for Computational Neuroscience, funded by German Federal Ministry of Education and Research Grant BMBF/FKZ 01GQ1002 (M.O.), and the European Research Council (ERC) under the European Union's Horizon 2020 research and innovation program (grant agreement No 633428) (M.O.). We thank Madeleine Junkins for technical assistance and Margot Elmaleh, Elnaz Hozhabri, and Kalman Katlowitz for comments on earlier versions of this manuscript.

References

Ankerst M, Breunig MM, Kriegel HP, Sander J. OPTICS: Ordering points to identify the clustering structure. Sigmod Record. 1999; 28(2):49–60. June 1999.

Armstrong E, Abarbanel HD. Model of the songbird nucleus HVC as a network of central pattern generators. J Neurophysiol. 2016; 116(5):2405–2419. DOI: 10.1152/jn.00438.2016 [PubMed: 27535375]

Basista MJ, Elliott KC, Wu W, Hyson RL, Bertram R, Johnson F. Independent premotor encoding of the sequence and structure of birdsong in avian cortex. J Neurosci. 2014; 34(50):16821–16834. DOI: 10.1523/JNEUROSCI.1940-14.2014 [PubMed: 25505334]

Benton S, Cardin JA, DeVoogd TJ. Lucifer Yellow filling of area X-projecting neurons in the high vocal center of female canaries. Brain Res. 1998; 799(1):138–147. [PubMed: 9666104]

Bonke BA, Bonke D, Scheich H. Connectivity of the auditory forebrain nuclei in the guinea fowl (Numida meleagris). Cell Tissue Res. 1979; 200(1):101–121. [PubMed: 91442]

Bottjer SW, Glaessner SL, Arnold AP. Ontogeny of brain nuclei controlling song learning and behavior in zebra finches. J Neurosci. 1985; 5(6):1556–1562. [PubMed: 4009245]

Dercksen VJ, Hege HC, Oberlaender M. The Filament Editor: an interactive software environment for visualization, proof-editing and analysis of 3D neuron morphology. Neuroinformatics. 2014; 12(2): 325–339. DOI: 10.1007/s12021-013-9213-2 [PubMed: 24323305]

Dutar P, Vu HM, Perkel DJ. Multiple cell types distinguished by physiological, pharmacological, and anatomic properties in nucleus HVc of the adult zebra finch. J Neurophysiol. 1998; 80(4):1828–1838. [PubMed: 9772242]

Fortune ES, Margoliash D. Cytoarchitectonic Organization and Morphology of Cells of the Field-L Complex in Male Zebra Finches (Taenopygia-Guttata). Journal of Comparative Neurology. 1992; 325(3):388–404. DOI: 10.1002/cne.903250306 [PubMed: 1447407]

Fortune ES, Margoliash D. Parallel pathways and convergence onto HVc and adjacent neostriatum of adult zebra finches (Taeniopygia guttata). J Comp Neurol. 1995; 360(3):413–441. DOI: 10.1002/cne.903600305 [PubMed: 8543649]

Galvis D, Wu W, Hyson RL, Johnson F, Bertram R. A distributed neural network model for the distinct roles of medial and lateral HVC in zebra finch song production. J Neurophysiol. 2017; 118(2): 677–692. DOI: 10.1152/jn.00917.2016 [PubMed: 28381490]

Gibb L, Gentner TQ, Abarbanel HD. Inhibition and recurrent excitation in a computational model of sparse bursting in song nucleus HVC. J Neurophysiol. 2009; 102(3):1748–1762. DOI: 10.1152/jn.00670.2007 [PubMed: 19515949]

Goller F, Cooper BG. Peripheral motor dynamics of song production in the zebra finch. Ann N Y Acad Sci. 2004; 1016:130–152. DOI: 10.1196/annals.1298.009 [PubMed: 15313773]

Guest JM, Seetharama MM, Wendel ES, Strick PL, Oberlaender M. 3D reconstruction and standardization of the rat facial nucleus for precise mapping of vibrissal motor networks. Neuroscience. 2017; doi: 10.1016/j.neuroscience.2017.09.031

Hahnloser RH, Kozhevnikov AA, Fee MS. An ultra-sparse code underlies the generation of neural sequences in a songbird. Nature. 2002; 419(6902):65–70. DOI: 10.1038/nature00974 [PubMed: 12214232]

Hamaguchi K, Tanaka M, Mooney R. A Distributed Recurrent Network Contributes to Temporally Precise Vocalizations. Neuron. 2016; 91(3):680–693. DOI: 10.1016/j.neuron.2016.06.019 [PubMed: 27397518]

Hamaguchi K, Tschida KA, Yoon I, Donald BR, Mooney R. Auditory synapses to song premotor neurons are gated off during vocalization in zebra finches. Elife. 2014; 3:e01833.doi: 10.7554/eLife.01833 [PubMed: 24550254]

Hanuschkin A, Diesmann M, Morrison A. A reafferent and feed-forward model of song syntax generation in the Bengalese finch. J Comput Neurosci. 2011; 31(3):509–532. DOI: 10.1007/s10827-011-0318Cz [PubMed: 21404048]

Harvey CD, Coen P, Tank DW. Choice-specific sequences in parietal cortex during a virtual-navigation decision task. Nature. 2012; 484(7392):62–68. DOI: 10.1038/nature10918 [PubMed: 22419153]

Jin DZ. Generating variable birdsong syllable sequences with branching chain networks in avian premotor nucleus HVC. Phys Rev E Stat Nonlin Soft Matter Phys. 2009; 80(5 Pt 1):051902.doi: 10.1103/PhysRevE.80.051902 [PubMed: 20365001]

Karten HJ. The ascending auditory pathway in the pigeon (Columba livia). II. Telencephalic projections of the nucleus ovoidalis thalami. Brain Res. 1968; 11(1):134–153. [PubMed: 5749228]

Katz LC, Gurney ME. Auditory responses in the zebra finch's motor system for song. Brain Res. 1981; 221(1):192–197. [PubMed: 6168335]

Kelley DB, Nottebohm F. Projections of a telencephalic auditory nucleus-field L-in the canary. J Comp Neurol. 1979; 183(3):455–469. DOI: 10.1002/cne.901830302 [PubMed: 759444]

KittelbergerJM. Neurotrophins, Synaptic Connectivity and the Regulation of Song Plasticity in the Zebra FinchDuke University; 2002Doctor of Philosophy3077141

Kornfeld J, Benezra SE, Narayanan RT, Svara F, Egger R, Oberlaender M, Long MA. EM connectomics reveals axonal target variation in a sequence-generating network. Elife. 2017; 6doi: 10.7554/eLife.24364

Kosche G, Vallentin D, Long MA. Interplay of inhibition and excitation shapes a premotor neural sequence. J Neurosci. 2015; 35(3):1217–1227. DOI: 10.1523/JNEUROSCI.4346-14.2015 [PubMed: 25609636]

Kozhevnikov AA, Fee MS. Singing-related activity of identified HVC neurons in the zebra finch. J Neurophysiol. 2007; 97(6):4271–4283. DOI: 10.1152/jn.00952.2006 [PubMed: 17182906]

Kubota M, Taniguchi I. Electrophysiological characteristics of classes of neuron in the HVc of the zebra finch. J Neurophysiol. 1998; 80(2):914–923. [PubMed: 9705478]

Long MA, Jin DZ, Fee MS. Support for a synaptic chain model of neuronal sequence generation. Nature. 2010; 468(7322):394–399. DOI: 10.1038/nature09514 [PubMed: 20972420]

Lynch GF, Okubo TS, Hanuschkin A, Hahnloser RH, Fee MS. Rhythmic Continuous-Time Coding in the Songbird Analog of Vocal Motor Cortex. Neuron. 2016; 90(4):877–892. DOI: 10.1016/j.neuron.2016.04.021 [PubMed: 27196977]

Mello CV, Vates GE, Okuhata S, Nottebohm F. Descending auditory pathways in the adult male zebra finch (Taeniopygia guttata). J Comp Neurol. 1998; 395(2):137–160. [PubMed: 9603369]

Mello GB, Soares S, Paton JJ. A scalable population code for time in the striatum. Curr Biol. 2015; 25(9):1113–1122. DOI: 10.1016/j.cub.2015.02.036 [PubMed: 25913405]

Mooney R. Different subthreshold mechanisms underlie song selectivity in identified HVc neurons of the zebra finch. J Neurosci. 2000; 20(14):5420–5436. [PubMed: 10884326]

Mooney R, Prather JF. The HVC microcircuit: the synaptic basis for interactions between song motor and vocal plasticity pathways. J Neurosci. 2005; 25(8):1952–1964. DOI: 10.1523/JNEUROSCI.3726-04.2005 [PubMed: 15728835]

Narayanan RT, Egger R, Johnson AS, Mansvelder HD, Sakmann B, de Kock CP, Oberlaender M. Beyond Columnar Organization: Cell Type- and Target Layer-Specific Principles of Horizontal Axon Projection Patterns in Rat Vibrissal Cortex. Cereb Cortex. 2015; 25(11):4450–4468. DOI: 10.1093/cercor/bhv053 [PubMed: 25838038]

Narayanan RT, Mohan H, Broersen R, de Haan R, Pieneman AW, de Kock CP. Juxtasomal biocytin labeling to study the structure-function relationship of individual cortical neurons. J Vis Exp. 2014; (84):e51359.doi: 10.3791/51359 [PubMed: 24638127]

Nixdorf BE, Davis SS, DeVoogd TJ. Morphology of Golgi-impregnated neurons in hyperstriatum ventralis, pars caudalis in adult male and female canaries. J Comp Neurol. 1989; 284(3):337–349. DOI: 10.1002/cne.902840302 [PubMed: 2474004]

Nottebohm F, Kelley DB, Paton JA. Connections of vocal control nuclei in the canary telencephalon. J Comp Neurol. 1982; 207(4):344–357. DOI: 10.1002/cne.902070406 [PubMed: 7119147]

Nottebohm F, Stokes TM, Leonard CM. Central control of song in the canary, Serinus canarius. J Comp Neurol. 1976; 165(4):457–486. DOI: 10.1002/cne.901650405 [PubMed: 1262540]

Oberlaender M, Bruno RM, Sakmann B, Broser PJ. Transmitted light brightfield mosaic microscopy for three-dimensional tracing of single neuron morphology. J Biomed Opt. 2007; 12(6): 064029.doi: 10.1117/1.2815693 [PubMed: 18163845]

Oberlaender M, de Kock CP, Bruno RM, Ramirez A, Meyer HS, Dercksen VJ, Sakmann B. Cell type-specific three-dimensional structure of thalamocortical circuits in a column of rat vibrissal cortex. Cereb Cortex. 2012; 22(10):2375–2391. DOI: 10.1093/cercor/bhr317 [PubMed: 22089425]

Oberlaender M, Dercksen VJ, Egger R, Gensel M, Sakmann B, Hege HC. Automated three-dimensional detection and counting of neuron somata. J Neurosci Methods. 2009; 180(1):147–160. DOI: 10.1016/j.jneumeth.2009.03.008 [PubMed: 19427542]

Pastalkova E, Itskov V, Amarasingham A, Buzsaki G. Internally generated cell assembly sequences in the rat hippocampus. Science. 2008; 321(5894):1322–1327. DOI: 10.1126/science.1159775 [PubMed: 18772431]

Picardo MA, Merel J, Katlowitz KA, Vallentin D, Okobi DE, Benezra SE, Long MA. Population-Level Representation of a Temporal Sequence Underlying Song Production in the Zebra Finch. Neuron. 2016; 90(4):866–876. DOI: 10.1016/j.neuron.2016.02.016 [PubMed: 27196976]

Pinault D. A novel single-cell staining procedure performed in vivo under electrophysiological control: morpho-functional features of juxtacellularly labeled thalamic cells and other central neurons with biocytin or Neurobiotin. J Neurosci Methods. 1996; 65(2):113–136. [PubMed: 8740589]

Poole B, Markowitz JE, Gardner TJ. The song must go on: resilience of the songbird vocal motor pathway. PLoS One. 2012; 7(6):e38173.doi: 10.1371/journal.pone.0038173 [PubMed: 22768040]

Roberts TF, Hisey E, Tanaka M, Kearney MG, Chattree G, Yang CF, Mooney R. Identification of a motor-to-auditory pathway important for vocal learning. Nat Neurosci. 2017; 20(7):978–986. DOI: 10.1038/nn.4563 [PubMed: 28504672]

Rojas-Piloni G, Guest JM, Egger R, Johnson AS, Sakmann B, Oberlaender M. Relationships between structure, in vivo function and long-range axonal target of cortical pyramidal tract neurons. Nat Commun. 2017; 8(1):870.doi: 10.1038/s41467-017-00971-0 [PubMed: 29021587]

Scharff C, Kirn JR, Grossman M, Macklis JD, Nottebohm F. Targeted neuronal death affects neuronal replacement and vocal behavior in adult songbirds. Neuron. 2000; 25(2):481–492. [PubMed: 10719901]

Scharff C, Nottebohm F. A comparative study of the behavioral deficits following lesions of various parts of the zebra finch song system: implications for vocal learning. J Neurosci. 1991; 11(9): 2896–2913. [PubMed: 1880555]

Schmidt H, Gour A, Straehle J, Boergens KM, Brecht M, Helmstaedter M. Axonal synapse sorting in medial entorhinal cortex. Nature. 2017; 549(7673):469–475. DOI: 10.1038/nature24005 [PubMed: 28959971]

Schmitt LI, Wimmer RD, Nakajima M, Happ M, Mofakham S, Halassa MM. Thalamic amplification of cortical connectivity sustains attentional control. Nature. 2017; 545(7653):219–223. DOI: 10.1038/nature22073 [PubMed: 28467827]

Sohrabji F, Nordeen EJ, Nordeen KW. Selective impairment of song learning following lesions of a forebrain nucleus in the juvenile zebra finch. Behav Neural Biol. 1990; 53(1):51–63. [PubMed: 2302141]

Stauffer TR, Elliott KC, Ross MT, Basista MJ, Hyson RL, Johnson F. Axial organization of a brain region that sequences a learned pattern of behavior. J Neurosci. 2012; 32(27):9312–9322. DOI: 10.1523/JNEUROSCI.0978-12.2012 [PubMed: 22764238]

Vallentin D, Long MA. Motor origin of precise synaptic inputs onto forebrain neurons driving a skilled behavior. J Neurosci. 2015; 35(1):299–307. DOI: 10.1523/JNEUROSCI.3698-14.2015 [PubMed: 25568122]

Vates GE, Broome BM, Mello CV, Nottebohm F. Auditory pathways of caudal telencephalon and their relation to the song system of adult male zebra finches. J Comp Neurol. 1996; 366(4):613–642. 4<613::AIDC CNE5>3.0.CO;2-7. DOI: 10.1002/(SICI)1096-9861(19960318)366 [PubMed: 8833113]

Walton C, Pariser E, Nottebohm F. The zebra finch paradox: song is little changed, but number of neurons doubles. J Neurosci. 2012; 32(3):761–774. DOI: 10.1523/JNEUROSCI.3434-11.2012 [PubMed: 22262875]

Wang N, Hurley P, Pytte C, Kirn JR. Vocal control neuron incorporation decreases with age in the adult zebra finch. J Neurosci. 2002; 22(24):10864–10870. [PubMed: 12486180]

Wild JM. Descending projections of the songbird nucleus robustus archistriatalis. J Comp Neurol. 1993; 338(2):225–241. DOI: 10.1002/cne.903380207 [PubMed: 8308169]

Yip ZC, Miller-Sims VC, Bottjer SW. Morphology of axonal projections from the high vocal center to vocal motor cortex in songbirds. J Comp Neurol. 2012; 520(12):2742–2756. DOI: 10.1002/cne.23084 [PubMed: 22684940]

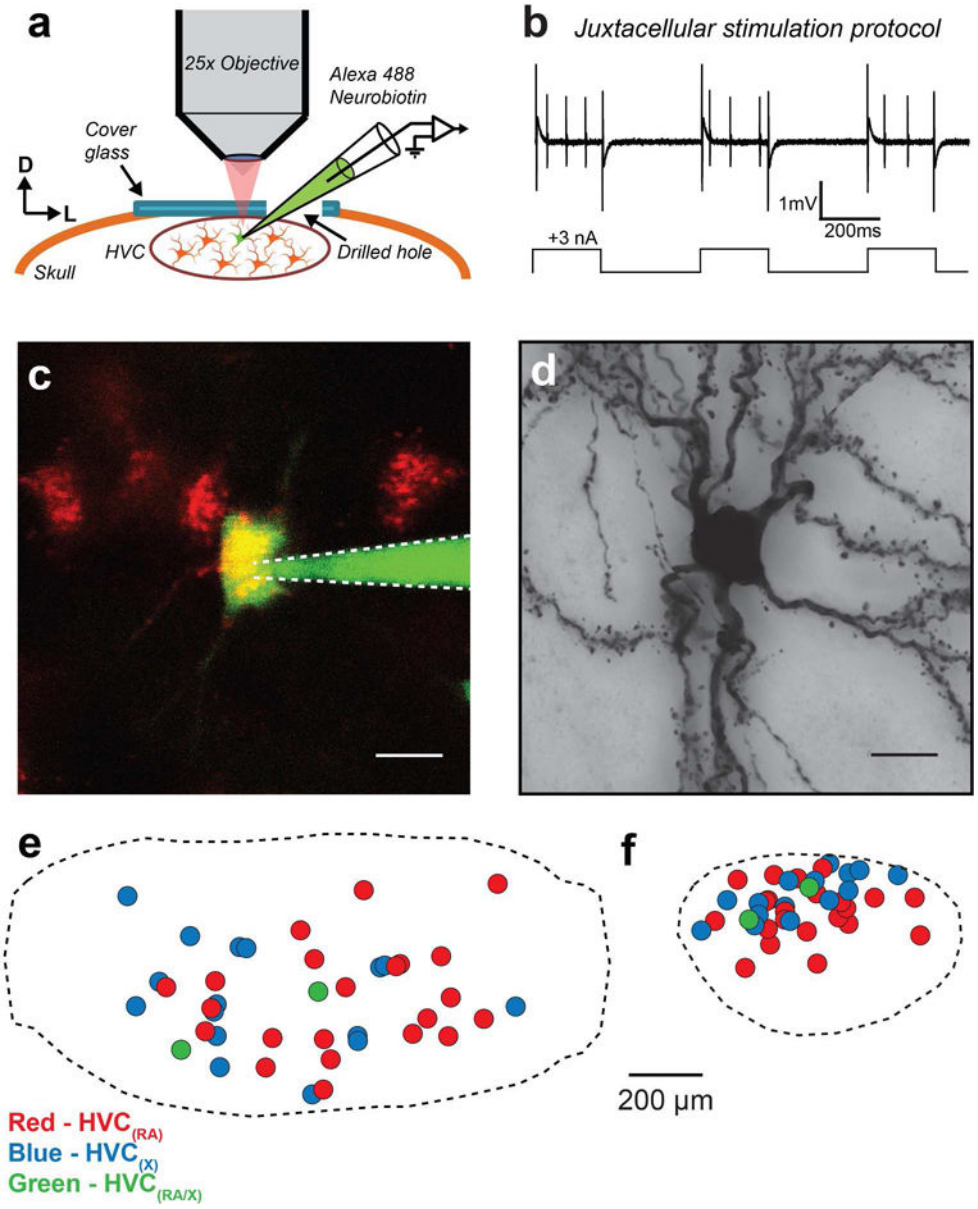

FIGURE 1. Two-photon guided single-cell filling

(a) *In vivo* imaging preparation for targeted cell fills. $HVC_{(RA)}$ or $HVC_{(X)}$ neurons are targeted under visual guidance through a cover glass implanted over HVC. (b) In a juxtacellular configuration, positive current pulses are used to fill neurons with Neurobiotin, often eliciting spikes. (c) Example image of a cell being filled with Alexa 488 and Neurobiotin *in vivo*. (d) Brightfield micrograph of the filled neuron in (c) after histological processing. Scale bars: 10 µm. (e) Relative locations of 40 reconstructed somata mapped onto an average HVC reference frame such that the long axis of HVC is defined along the horizontal. (f) An orthogonal view perpendicular to the long axis of HVC.

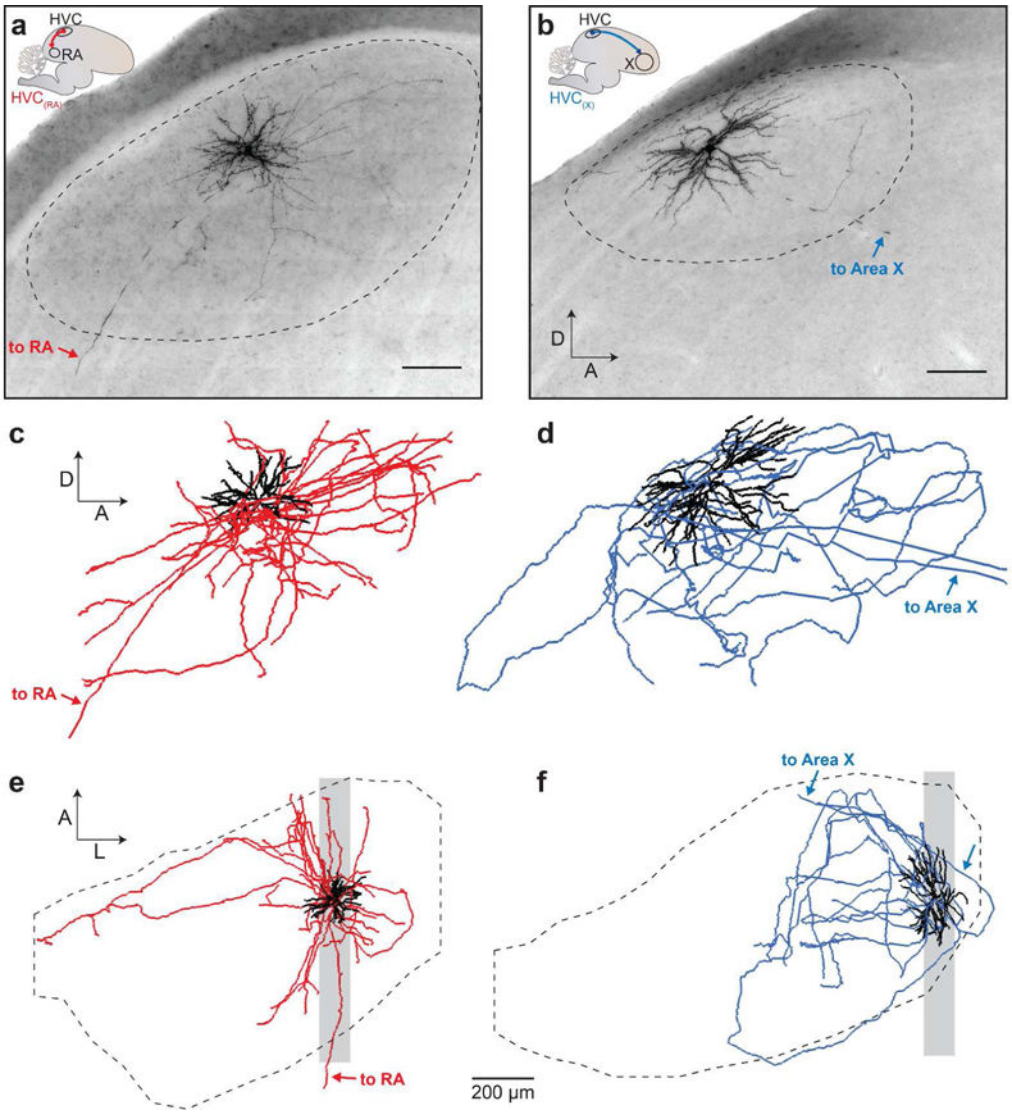

FIGURE 2. Anatomical reconstruction of HVC projection neurons

(a, b) Micrographs show a projection of 100 µm sagittal sections of a DAB-stained $HVC_{(RA)}$ neuron (a) and $HVC_{(X)}$ neuron (b). Scalebars: 100 µm. (c, d) Complete reconstructions of the above neurons shown in the sagittal plane. Scale of reconstructions is matched with micrographs in (a, b). (e, f) Same cells as in (c) and (d), shown in the horizontal plane. Shaded region marks the area shown in the micrographs (a,b). Dendrites are represented with black lines, and axons are either red ($HVC_{(RA)}$) (a) or blue ($HVC_{(X)}$) (B). Dotted lines mark HVC boundaries in (a, b, e, f). Arrows indicate descending axons.

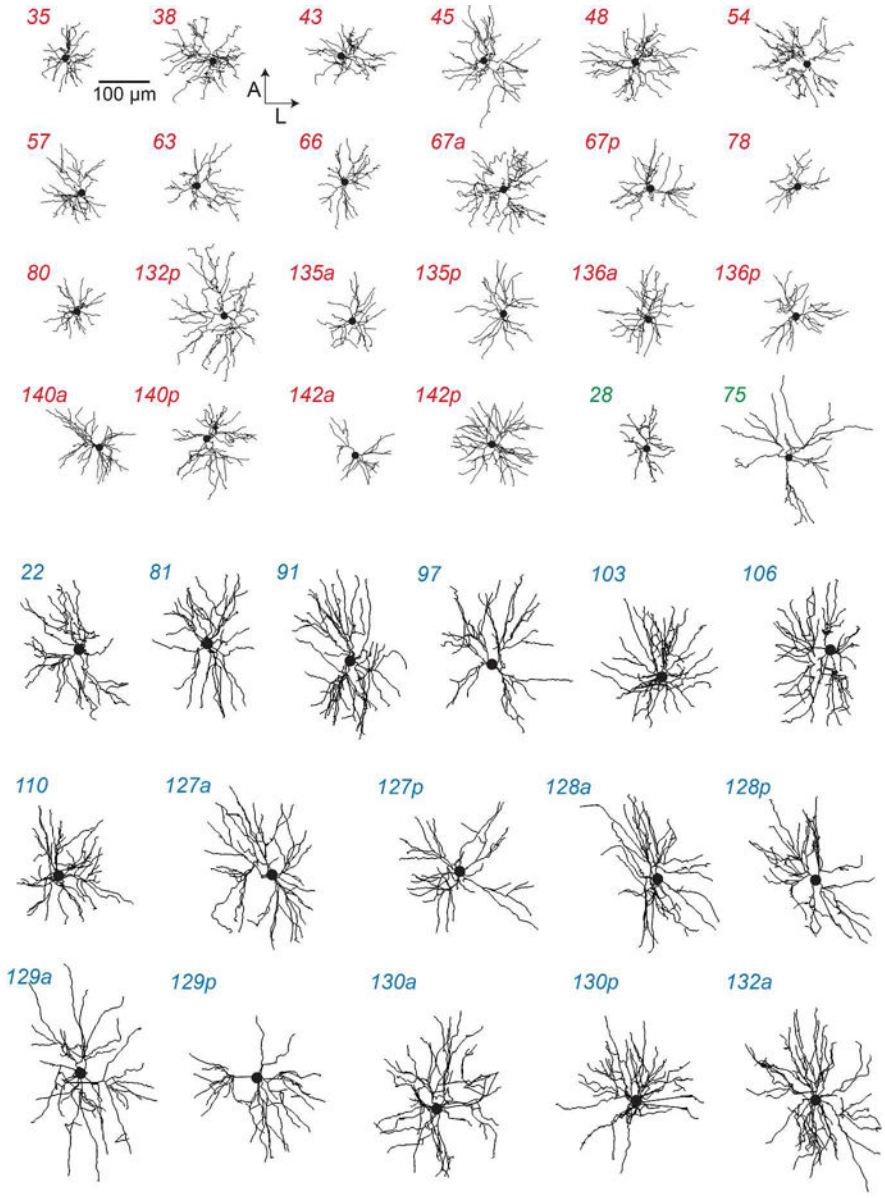

FIGURE 3. Dendrites of HVC projection neurons

Each panel shows the dendrite of an $HVC_{(RA)}$ (red), $HVC_{(RA/X)}$ (green) or $HVC_{(X)}$ (blue) neuron projected on the horizontal plane. All $HVC_{(RA)}$ neurons are designated as 'compact' with the exception of 132p, and all $HVC_{(X)}$ neurons were designated as 'large' (see Figure 4 and Materials and Methods). One $HVC_{(RA/X)}$ neuron each fell into the 'compact' and 'large' categories.

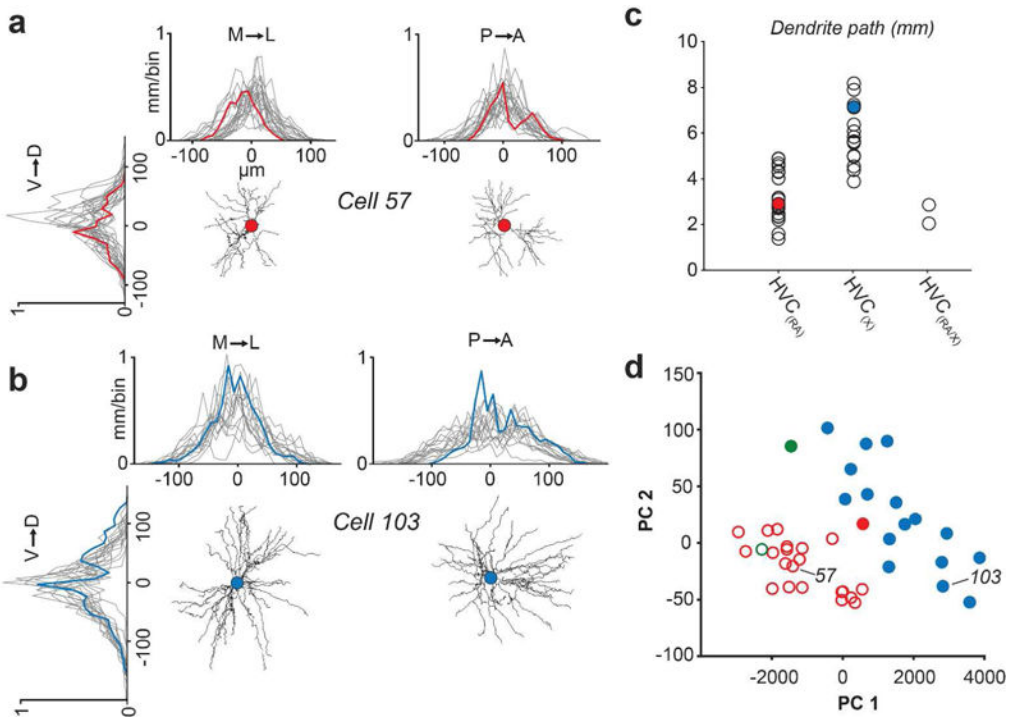

FIGURE 4. Spatial properties of $HVC_{(RA)}$ and $HVC_{(X)}$ dendrites

(a, b) One dimensional profile of dendritic length along three axes for $HVC_{(RA)}$ (a) and $HVC_{(X)}$ (b) neurons. Red and blue traces are from example neurons, grey traces are from all remaining individual neurons from each group in our data set. The center of each plot (0 μm) denotes soma location. (c) Total dendritic path length organized by projection target. Filled circles represent examples from (a) and (b). (d) The first two principal components of four spatial parameters of dendrites. The two clusters as designated using the OPTICS algorithm (see Materials and Methods) are represented by closed circles and open circles; Red - $HVC_{(RA)}$; Blue - $HVC_{(X)}$; Green - HVC(RA/X).

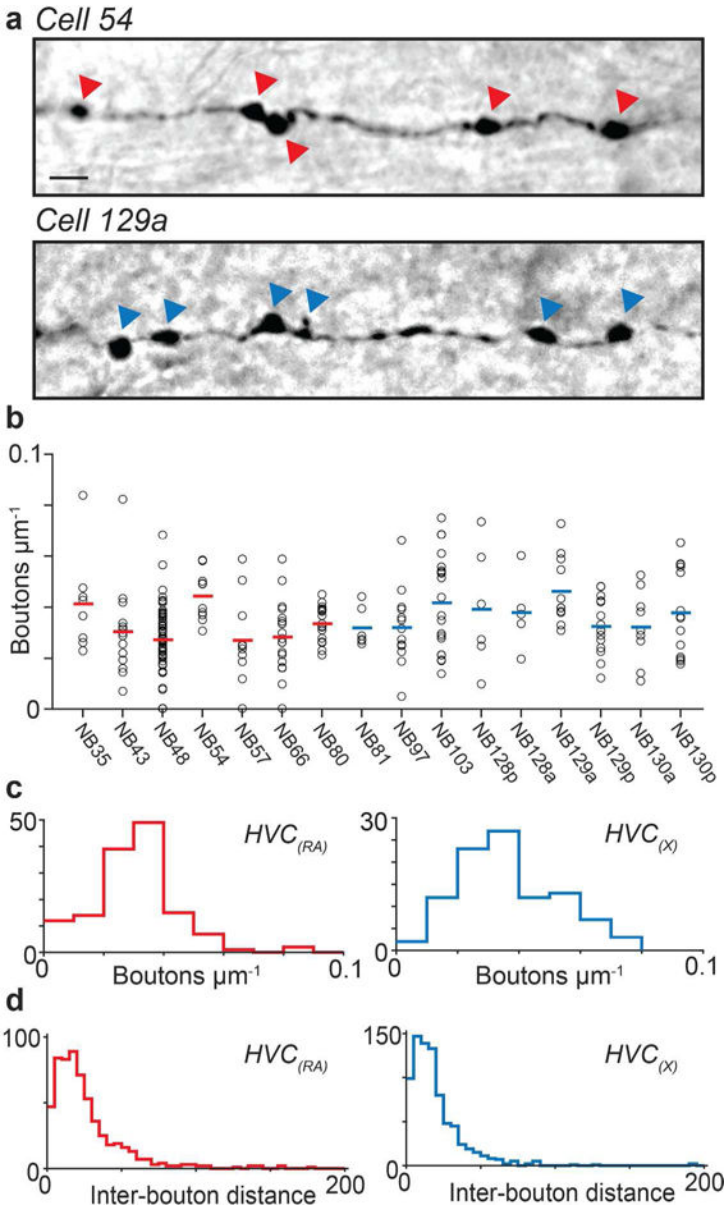

FIGURE 5. Bouton density of $HVC_{(RA)}$ and $HVC_{(X)}$ collaterals

(a) Example micrographs of $HVC_{(RA)}$ (top) and $HVC_{(X)}$ (bottom) axon collaterals. Scale bar: 5 µm. Arrowheads mark the location of boutons. (b) Bouton densities from 170 branches in 7 $HVC_{(RA)}$ neurons and 95 branches in 9 $HVC_{(X)}$ neurons. Mean density for each cell is shown as red and blue horizontal line, respectively. (c, d) Histograms showing bouton densities for all branches (c) as well as inter-bouton distance (d) for each cell type from (b).

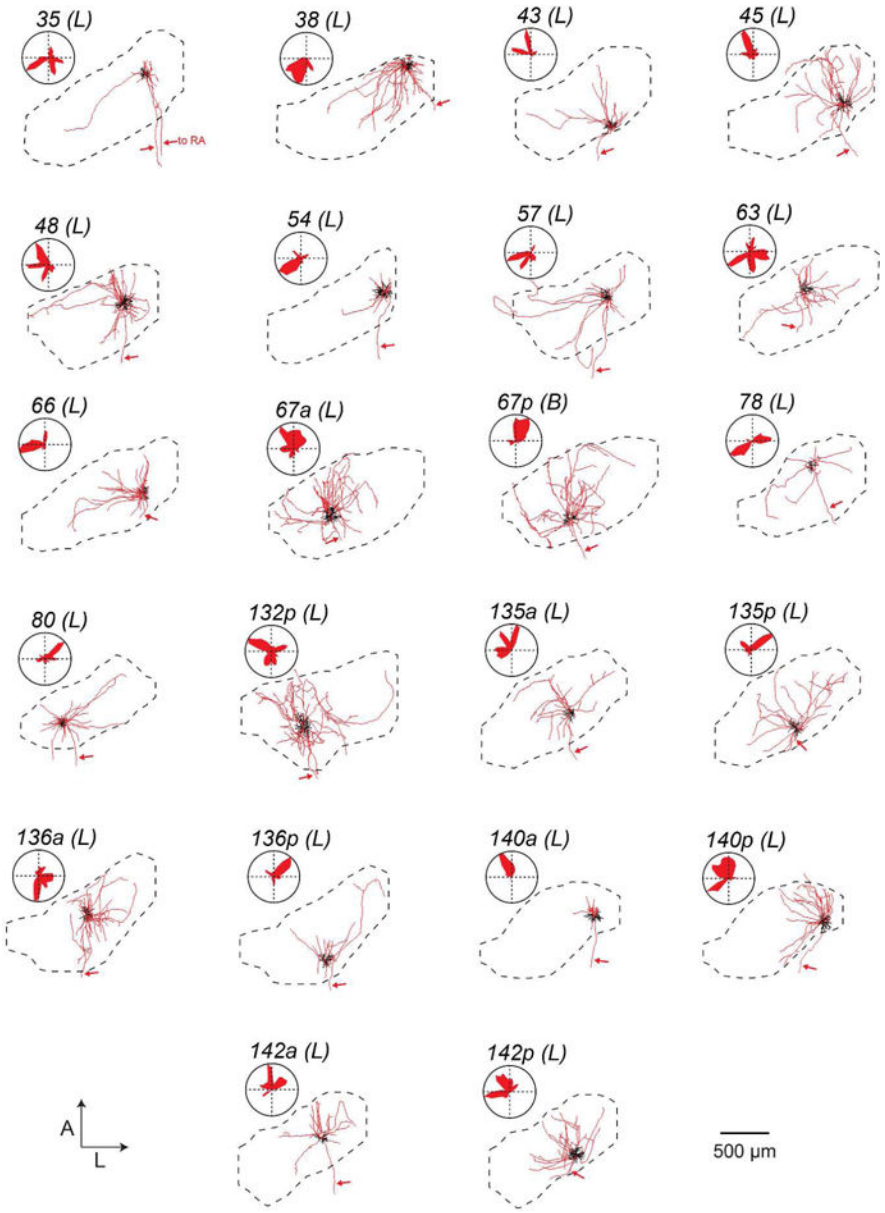

FIGURE 6. Local processes of HVC$_{(RA)}$ neurons

Each panel shows the dendrite (black) and local axons (red) of all HVC$_{(RA)}$ neurons projected on the horizontal plane and its position within HVC with accompanying polar plots quantifying axonal distribution. Arrows mark descending axons to RA. 'Local' (L) and 'broadcast' (B) designations given in parentheses (see Figure 11 and Materials and Methods).

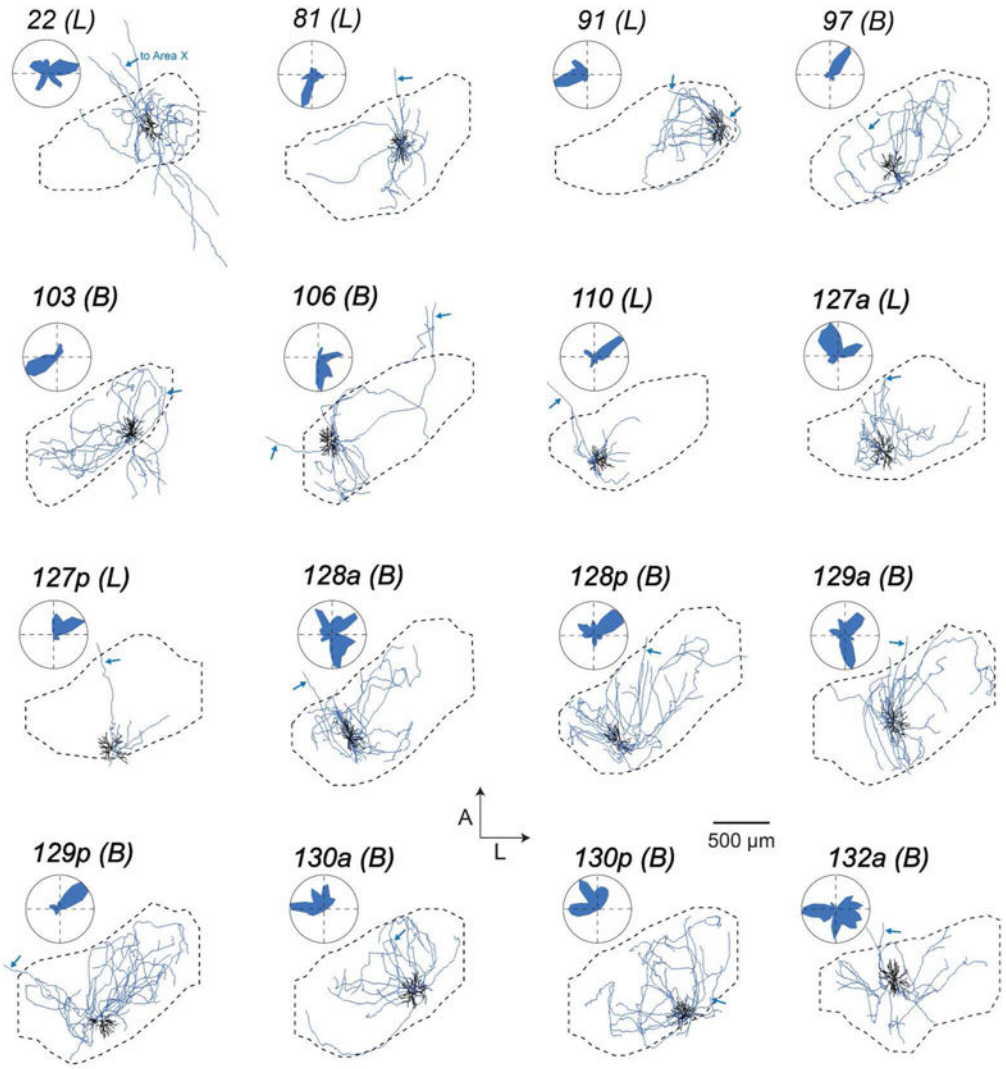

FIGURE 7. Local processes of $HVC_{(X)}$ neurons

Each panel shows the dendrite (black) and local axons (blue) of all $HVC_{(X)}$ neurons projected on the horizontal plane and its position within HVC with accompanying polar plots quantifying axonal distribution. Arrows mark descending axon to Area X. 'Local' (L) and 'broadcast' (B) designations given in parentheses (see Figure 11 and Materials and Methods).

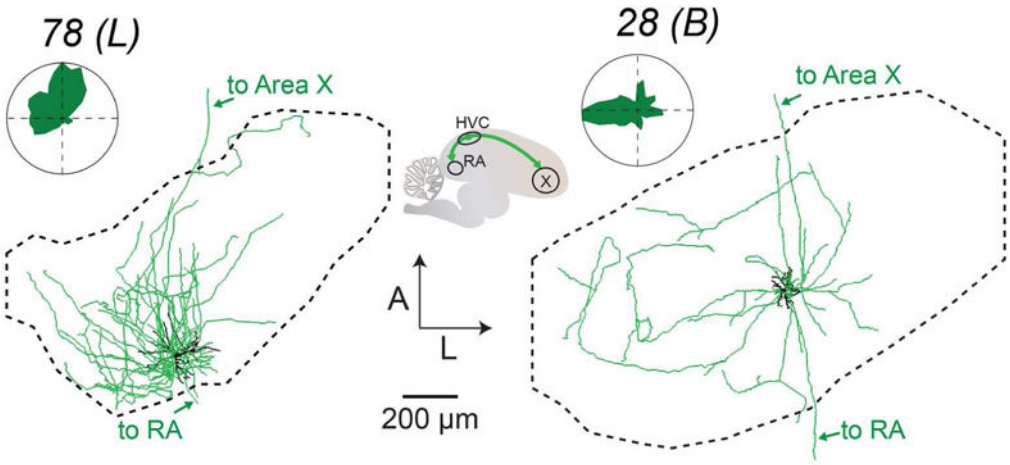

FIGURE 8. Local processes of $HVC_{(RA/X)}$ neurons

Each panel shows the dendrite (black) and local axons (green) of both $HVC_{(RA/X)}$ neurons projected on the horizontal plane and its position within HVC with accompanying polar plots quantifying axonal distribution. Arrows mark descending axons to RA and Area X. 'Local' (L) and 'broadcast' (B) designations given in parentheses (see Figure 11 and Materials and Methods).

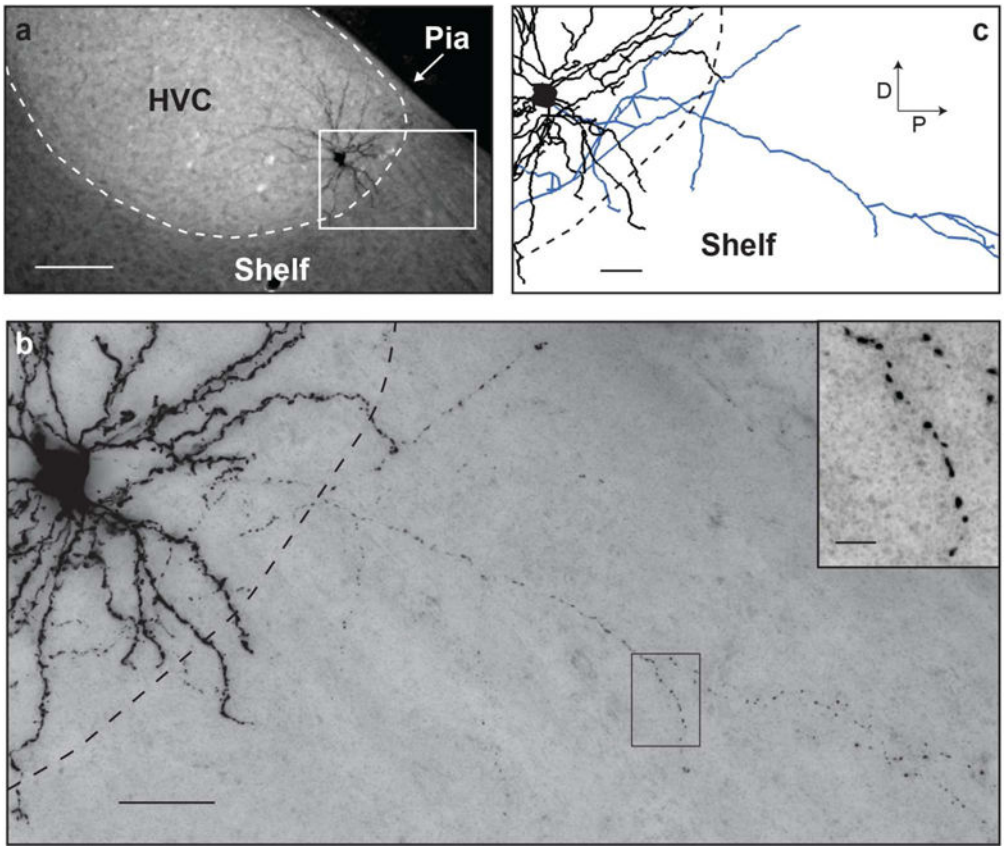

FIGURE 9. $HVC_{(X)}$ dendrites and collaterals can extend into HVC shelf

(a) Fluorescent micrograph of a sagittal section of Cell 103. Scale bar: 100 μm. (b) Brightfield micrograph of the area indicated with a white rectangle in (a). Inset shows a high magnification image from the boxed region. Scale bars: 25 μm and 5 μm (inset). (c) Reconstructed dendrite (black) and axon collaterals (blue) from the boxed region in (a). Scale bar: 25 μm.

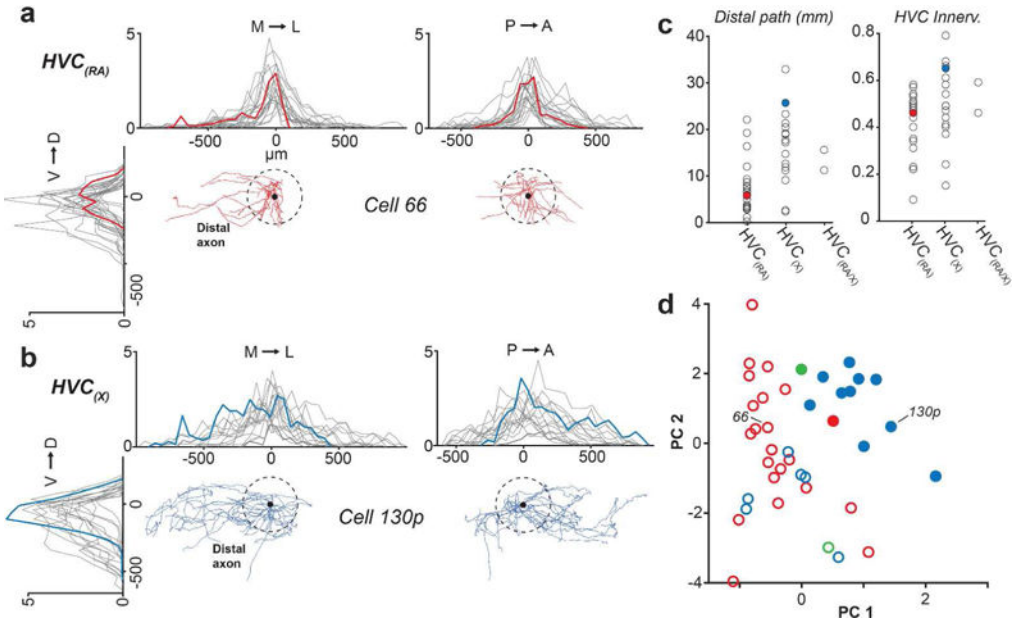

FIGURE 10. Spatial properties of $HVC_{(RA)}$ and $HVC_{(X)}$ axons

(a, b) One dimensional profile of axonal length along three axes for $HVC_{(RA)}$ (a) and $HVC_{(X)}$ (b) neurons. Red and blue traces are from example neurons, grey traces are from all remaining individual neurons from each group in our data set. The center of each plot (0 μm) denotes soma location. (c) Distal axon path length and HVC innervation proportion (see Materials and Methods) organized by projection target. Filled circles represent examples from (A) and (B). (d) The first two principal components of four spatial parameters of axons. The two clusters as designated using the OPTICS algorithm (see Materials and Methods) are represented by closed circles and open circles; Red - $HVC_{(RA)}$; Blue - $HVC_{(X)}$; Green - $HVC_{(RA/X)}$.

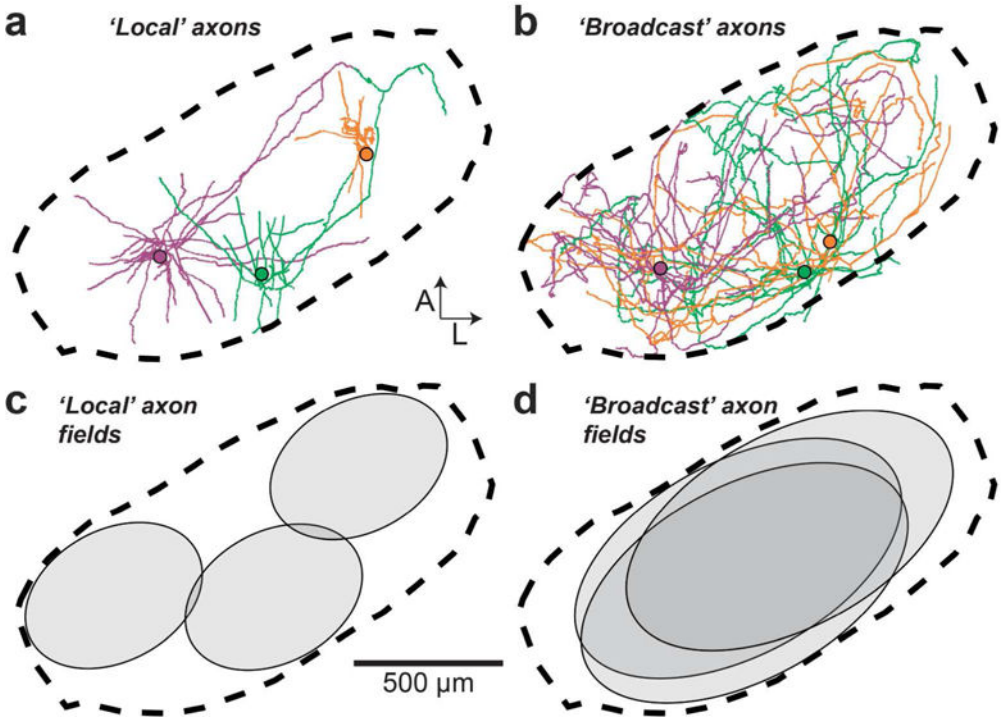

FIGURE 11. Broadcast axons innervate a larger volume than local axons

(a, b) Axons of three local (a) and broadcast (b) neurons registered within the average HVC reference frame (dotted line). (c, d) Schematic of local (c) and broadcast (d) axonal innervation of HVC.

Table 1

Features of HVC projection neuron dendrites. Statistical differences were assessed using the Wilcoxon rank-sum test.

ID	Proj. target	90% M-L extent (μm)	90% A-P extent (μm)	90% D-V extent (μm)	90% radial extent (μm)	Path length (mm)	Primary branches	Branch nodes	Dendrite cluster
35	RA	60	90	90	68	2.78	5	35	Small
38	RA	120	100	110	88	4.27	7	53	Small
43	RA	110	70	110	82	3.15	5	55	Small
45	RA	140	130	110	102	4.00	6	44	Small
48	RA	130	100	90	85	4.53	7	52	Small
54	RA	120	120	120	98	4.84	5	58	Small
57	RA	80	100	90	80	2.88	4	39	Small
63	RA	110	90	130	98	2.72	3	37	Small
66	RA	80	110	120	84	2.72	6	30	Small
67a	RA	110	110	70	84	4.64	5	70	Small
67p	RA	110	80	70	78	2.68	6	32	Small
78	RA	80	70	100	70	1.56	8	20	Small
80	RA	60	70	100	68	2.31	5	37	Small
132p	RA	120	180	110	122	4.86	4	40	Large
135a	RA	70	100	100	77	2.32	4	29	Small
135p	RA	80	120	110	87	2.45	4	38	Small
136a	RA	90	120	100	89	3.15	6	42	Small
136p	RA	110	100	50	72	2.18	5	38	Small
140a	RA	100	100	110	88	3.07	6	40	Small
140p	RA	100	110	120	92	4.30	3	53	Small
142a	RA	90	80	60	66	1.35	4	20	Small
142p	RA	110	100	70	81	4.27	8	69	Small
AVG±SD		99±22	102±24	97±21	85±13	3.23±1.06	5.3±1.4	42±13	
22	X	160	190	160	134	4.99	4	47	Large
81	X	110	190	180	137	5.61	12	23	Large
91	X	120	220	120	130	7.09	5	64	Large

J Comp Neurol. Author manuscript; available in PMC 2019 July 01.

ID	Proj. target	90% M-L extent (μm)	90% A-P extent (μm)	90% D-V extent (μm)	90% radial extent (μm)	Path length (mm)	Primary branches	Branch nodes	Dendrite cluster
97	X	150	240	160	152	4.95	6	47	Large
103	X	130	190	180	129	7.12	10	67	Large
106	X	140	210	110	131	6.04	7	56	Large
110	X	140	150	160	123	5.59	6	49	Large
127a	X	160	210	170	144	6.34	4	52	Large
127p	X	160	160	150	135	4.36	7	30	Large
128a	X	140	220	150	140	5.80	5	60	Large
128p	X	160	200	130	133	4.52	4	60	Large
129a	X	160	260	140	153	5.54	6	49	Large
129p	X	180	210	100	131	3.86	4	37	Large
130a	X	170	220	160	150	7.23	11	59	Large
130p	X	170	180	160	130	7.88	4	83	Large
132a	X	190	220	150	147	8.15	10	87	Large
AVG±SD		153±21	204±28	149±23	137±9	5.94±1.27	6.6±2.7	54±17	
RA vs. X p-val.		$1.7*10^{-6}$	$2.7*10^{-7}$	$4.9*10^{-6}$	$2.1*10^{-7}$	$2.4*10^{-6}$	0.25	0.03	
28	RA/X	60	100	90	71	2.01	4	25	Small
75	RA/X	170	150	180	142	2.83	7	28	Large
Small AVG±SD		96±23	99±17	96±21	82±10	3.10±1.03	5.3±1.4	42±14	
Large AVG±SD		152±22	200±30	148±25	137±9	5.71±1.42	6.4±2.6	52±17	
Small vs. Large p-val.		$7.0*10^{-7}$	$6.7*10^{-8}$	$3.1*10^{-6}$	$7.8*10^{-8}$	$2.4*10^{-6}$	0.27	0.06	

Table 2

Features of HVC projection neuron axons. B: broadcast type, L: local type. Statistical differences were assessed using the Wilcoxon rank-sum test.

ID	Proj. target	90% M - L extent (μm)	90% A - P extent (μm)	90% D - V extent (μm)	Path length (mm)	Path length beyond 200 μm (mm)	Branch nodes beyond 25 μm	HVC innervation	Axon cluster
35	RA	800	250	350	6.77	2.74	24	0.23	L
38	RA	650	450	350	20.00	11.94	62	0.51	L
43	RA	600	450	150	7.35	2.99	22	0.22	L
45	RA	650	550	350	15.56	9.21	42	0.51	L
48	RA	600	500	200	16.66	7.81	73	0.57	L
54	RA	350	200	250	5.89	1.06	18	0.22	L
57	RA	850	500	300	10.83	5.72	27	0.49	L
63	RA	750	450	300	9.88	4.93	30	0.46	L
66	RA	700	350	300	12.42	5.73	38	0.46	L
67a	RA	750	500	400	24.36	19.17	44	0.47	L
67p	RA	900	700	350	22.24	16.28	37	0.50	B
78	RA	1000	350	300	5.97	3.21	13	0.40	L
80	RA	700	400	400	9.75	3.38	30	0.58	L
132p	RA	650	700	400	29.17	21.99	57	0.54	L
135a	RA	650	350	550	10.47	6.37	25	0.35	L
135p	RA	850	500	350	13.40	8.57	31	0.54	L
136a	RA	550	500	250	13.79	6.75	41	0.48	L
136p	RA	800	450	400	6.58	2.77	24	0.31	L
140a	RA	150	200	100	3.31	0.17	32	0.09	L
140p	RA	500	450	350	13.39	7.42	47	0.34	L
142a	RA	650	350	250	7.19	3.75	25	0.44	L
142p	RA	600	350	200	10.68	5.81	29	0.53	L
AVG±SD		668±184	432±131	311±99	12.53±6.61	7.17±5.66	36±14	0.42±0.13	
22	X	550	550	450	21.06	17.14	53	0.54	L
81	X	650	650	300	16.09	9.02	34	0.40	L
91	X	650	600	350	16.30	11.80	21	0.49	L

ID	Proj. target	90% M - L extent (μm)	90% A - P extent (μm)	90% D - V extent (μm)	Path length (mm)	Path length beyond 200 μm (mm)	Branch nodes beyond 25 μm	HVC innervation	Axon cluster
97	X	1150	600	400	22.35	18.89	39	0.66	B
103	X	1050	500	400	21.24	17.64	31	0.79	B
106	X	850	750	500	16.10	12.53	29	0.37	B
110	X	400	450	300	6.64	2.55	18	0.24	L
127a	X	650	550	250	15.39	11.09	38	0.41	L
127p	X	400	250	150	4.59	2.26	7	0.15	L
128a	X	950	650	400	27.06	21.23	51	0.49	B
128p	X	1200	600	450	30.37	23.20	48	0.58	B
129a	X	1100	800	450	26.69	20.39	47	0.47	B
129p	X	1150	550	450	38.88	32.81	58	0.68	B
130a	X	1050	700	350	22.80	19.03	32	0.61	B
130p	X	1100	700	350	32.07	25.60	52	0.65	B
132a	X	1000	650	350	17.90	14.64	27	0.44	B
AVG±SD		869±277	597±130	369±89	20.97±8.91	16.24±8.03	37±15	0.50±0.17	
RA vs. X p-val.		0.03	$4.2*10^{-4}$	0.046	0.003	0.002	0.52	0.15	
28	RA/X	950	600	300	16.07	11.15	39	0.46	B
75	RA/X	550	500	300	27.75	15.52	91	0.59	L
L AVG±SD		630±171	441±126	307±97	12.90±6.82	7.53±5.58	36±18	0.41±0.14	
B AVG±SD		1038±109	650±85	396±58	24.48±6.86	19.45±5.94	42±11	0.56±0.12	
B vs. L p-val.		$1.5*10^{-6}$	$2.4*10^{-5}$	0.003	$1.0*10^{-4}$	$2.6*10^{-5}$	0.11	0.01	